Dark-field hyperlens: Super-resolution imaging of weakly scattering objects

Repän, Taavi; Lavrinenko, Andrei; Zhukovsky, Sergei

Published in:
Optics Express

Link to article, DOI:
10.1364/OE.23.025350

Publication date:
2015

Document Version
Publisher's PDF, also known as Version of record

Dark-field hyperlens: Super-resolution imaging of weakly scattering objects

Taavi Repän,[1,2] **Andrei V. Lavrinenko,**[2,*] **and Sergei V. Zhukovsky**[2,3]

[1]*Institute of Physics, University of Tartu, Ravila 14c, Tartu 50411, Estonia*
[2]*DTU Fotonik, Technical University of Denmark, Ørsteds pl. 343, 2800 Kongens Lyngby, Denmark*
[3]*ITMO University, Kronverksky pr. 49, St. Petersburg, 197101, Russia*
**alav@fotonik.dtu.dk*

Abstract: We propose a device for subwavelength optical imaging based on a metal-dielectric multilayer hyperlens designed in such a way that only large-wavevector (evanescent) waves are transmitted while all propagating (small-wavevector) waves from the object area are blocked by the hyperlens. We numerically demonstrate that as the result of such filtering, the image plane only contains scattered light from subwavelength features of the objects and is completely free from background illumination. Similar in spirit to conventional dark-field microscopy, the proposed dark-field hyperlens is shown to enhance the subwavelength image contrast by more than two orders of magnitude. These findings are essential for optical imaging of weakly scattering subwavelength objects, such as real-time dynamic nanoscopy of label-free biological objects.

OCIS codes: (100.6640) Superresolution; (310.6628) Subwavelength structures, nanostructures; (160.3918) Metamaterials.

References and links

1. W. Cai and V. Shalaev, *Optical Metamaterials: Fundamentals and Applications* (Springer, 2009).
2. V. M. Shalaev, "Optical negative-index metamaterials," Nat. Photonics **1**, 41–48 (2007).
3. J. B. Pendry, "Negative refraction makes a perfect lens," Phys. Rev. Lett. **85**, 3966 (2000).
4. N. Fang, H. Lee, C. Sun, and X. Zhang, "Sub-diffraction-limited optical imaging with a silver superlens," Science **308**, 534–537 (2005).
5. Z. Liu, S. Durant, H. Lee, Y. Pikus, Y. Xiong, C. Sun, and X. Zhang, "Experimental studies of far-field superlens for sub-diffractional optical imaging," Opt. Express **15**, 6947–6954 (2007).
6. K. Aydin, I. Bulu, and E. Ozbay, "Subwavelength resolution with a negative-index metamaterial superlens," Appl. Phys. Lett. **90**, 254102 (2007).
7. Y. Xiong, Z. Liu, C. Sun, and X. Zhang, "Two-dimensional imaging by far-field superlens at visible wavelengths," Nano Lett. **7**, 3360–3365 (2007).
8. X. Zhang and Z. Liu, "Superlenses to overcome the diffraction limit," Nat. Mater. **7**, 435–441 (2008).
9. A. Poddubny, I. Iorsh, P. Belov, and Y. Kivshar, "Hyperbolic metamaterials," Nat. Photonics **7**, 948–957 (2013).
10. Z. Jacob, L. V. Alekseyev, and E. Narimanov, "Optical hyperlens: far-field imaging beyond the diffraction limit," Opt. Express **14**, 8247–8256 (2006).
11. Z. Liu, H. Lee, Y. Xiong, C. Sun, and X. Zhang, "Far-field optical hyperlens magnifying sub-diffraction-limited objects," Science **315**, 1686 (2007).
12. I. I. Smolyaninov, Y.-J. Hung, and C. C. Davis, "Magnifying superlens in the visible frequency range," Science **315**, 1699–1701 (2007).
13. J. Sun, M. I. Shalaev, and N. M. Litchinitser, "Experimental demonstration of a non-resonant hyperlens in the visible spectral range," Nat. Commun. **6**, 7201 (2015).
14. D. Lu and Z. Liu, "Hyperlenses and metalenses for far-field super-resolution imaging," Nat. Commun. **3**, 1205 (2012).

#244021 Received 16 Jul 2015; revised 30 Aug 2015; accepted 7 Sep 2015; published 18 Sep 2015

15. A. A. Orlov, I. V. Iorsh, S. V. Zhukovsky, and P. A. Belov, "Controlling light with plasmonic multilayers," Photonic Nanostruct. **12**, 213–230 (2014).
16. J. Rho, Z. Ye, Y. Xiong, X. Yin, Z. Liu, H. Choi, G. Bartal, and X. Zhang, "Spherical hyperlens for two-dimensional sub-diffractional imaging at visible frequencies," Nat. Commun. **1**, 143 (2010).
17. B. H. Cheng, Y.-C. Lan, and D. P. Tsai, "Breaking optical diffraction limitation using optical hybrid-super-hyperlens with radially polarized light," Opt. Express **21**, 14898–14906 (2013).
18. J. Li, L. Fok, X. Yin, G. Bartal, and X. Zhang, "Experimental demonstration of an acoustic magnifying hyperlens," Nat. Mater. **8**, 931–934 (2009).
19. A. Andryieuski, A. V. Lavrinenko, and D. N. Chigrin, "Graphene hyperlens for terahertz radiation," Phys. Rev. B **86**, 121108 (2012).
20. H. Hu, C. Ma, and Z. Liu, "Plasmonic dark field microscopy," Appl. Phys. Lett. **96**, 113107 (2010).
21. H. Benisty and F. Goudail, "Dark-field hyperlens exploiting a planar fan of tips," J. Opt. Soc. Am. B **29**, 2595–2602 (2012).
22. B. O. Leung and K. C. Chou, "Review of super-resolution fluorescence microscopy for biology," Appl. Spectrosc. **65**, 967–980 (2011).
23. S. Ayas, G. Cinar, A. D. Ozkan, Z. Soran, O. Ekiz, D. Kocaay, A. Tomak, P. Toren, Y. Kaya, I. Tunc, H. Zareie, T. Tekinay, A. B. Tekinay, M. O. Guler, and A. Dana, "Label-free nanometer-resolution imaging of biological architectures through surface enhanced raman scattering," Sci. Rep. **3**, 2624 (2013).
24. A. M. Wong and G. V. Eleftheriades, "An optical super-microscope for far-field, real-time imaging beyond the diffraction limit," Sci. Rep. **3**, 1715 (2013).
25. H. Yang, N. Moullan, J. Auwerx, and M. A. Gijs, "Super-resolution biological microscopy using virtual imaging by a microsphere nanoscope," Small **10**, 1712–1718 (2014).
26. D. R. Smith, D. Schurig, J. J. Mock, P. Kolinko, and P. Rye, "Partial focusing of radiation by a slab of indefinite media," Appl. Phys. Lett. **84**, 2244–2246 (2004).
27. O. Kidwai, S. V. Zhukovsky, and J. E. Sipe, "Effective-medium approach to planar multilayer hyperbolic metamaterials: Strengths and limitations," Phys. Rev. A **85**, 053842 (2012).
28. S. V. Zhukovsky, O. Kidwai, and J. E. Sipe, "Physical nature of volume plasmon polaritons in hyperbolic metamaterials," Opt. Express **21**, 14982–14987 (2013).
29. W. X. Jiang, C.-W. Qiu, T. C. Han, Q. Cheng, H. F. Ma, S. Zhang, and T. J. Cui, "Broadband all-dielectric magnifying lens for far-field high-resolution imaging," Adv. Mater. **25**, 6963–6968 (2013).
30. Y. Guo, W. Newman, C. L. Cortes, and Z. Jacob, "Applications of hyperbolic metamaterial substrates," Adv. Optoelectron. **2012**, 1–9 (2012).
31. S. Ishii, A. V. Kildishev, E. Narimanov, V. M. Shalaev, and V. P. Drachev, "Sub-wavelength interference pattern from volume plasmon polaritons in a hyperbolic medium," Laser Photonics Rev. **7**, 265–271 (2013).
32. K. G. Balmain and P. C. Kremer, "Resonance cone formation, reflection, refraction, and focusing in a planar anisotropic metamaterial," IEEE Antennas Wireless Propag. Lett. **1**, 146–149 (2002).
33. G. V. Eleftheriades and O. F. Siddiqui, "Negative refraction and focusing in hyperbolic transmission-line periodic grids," IEEE Trans. Microw. Theory Techn. **53**, 396–403 (2005).
34. P. A. Belov and Y. Hao, "Subwavelength imaging at optical frequencies using a transmission device formed by a periodic layered metal-dielectric structure operating in the canalization regime," Phys. Rev. B. **73**, 113110 (2006).
35. Y. Jin, "Improving subwavelength resolution of multilayered structures containing negative-permittivity layers by flatting the transmission curves," PIER. **105**, 347–364 (2010).
36. W. Yan, N. A. Mortensen, and M. Wubs, "Hyperbolic metamaterial lens with hydrodynamic nonlocal response," Opt. Express. **21**, 15027–15036 (2013).
37. S. H. Sedighy, C. Guclu, S. Campione, M. K. Amirhosseini, and F. Capolino, "Wideband planar transmission line hyperbolic metamaterial for subwavelength focusing and resolution," IEEE Trans. Microw. Theory Techn. **61**, 4110–4117 (2013).
38. N. I. Zheludev, "What diffraction limit?" Nat. Mater. **7**, 420–422 (2008).
39. S. V. Zhukovsky, A. Andryieuski, J. E. Sipe, and A. V. Lavrinenko, "From surface to volume plasmons in hyperbolic metamaterials: General existence conditions for bulk high-k waves in metal-dielectric and graphene-dielectric multilayers," Phys. Rev. B **90**, 155429 (2014).
40. X. Ni, S. Ishii, M. D. Thoreson, V. M. Shalaev, S. Han, S. Lee, and A. V. Kildishev, "Loss-compensated and active hyperbolic metamaterials," Opt. Express **19**, 25242–25254 (2011).
41. C. Argyropoulos, N. M. Estakhri, F. Monticone, and A. Alù, "Negative refraction, gain and nonlinear effects in hyperbolic metamaterials," Opt. Express **21**, 15037–15047 (2013).
42. A. J. Hoffman, L. Alekseyev, S. S. Howard, K. J. Franz, D. Wasserman, V. A. Podolskiy, E. E. Narimanov, D. L. Sivco, and C. Gmachl, "Negative refraction in semiconductor metamaterials," Nat. Mater. **6**, 946–950 (2007).
43. S. Campione, T. S. Luk, S. Liu, and M. B. Sinclair, "Realizing high-quality, ultralarge momentum states and ultrafast topological transitions using semiconductor hyperbolic metamaterials," J. Opt. Soc. Am. B **32**, 1809–1815 (2015).

#244021 Received 16 Jul 2015; revised 30 Aug 2015; accepted 7 Sep 2015; published 18 Sep 2015

1. Introduction

The recent decade in modern materials science has featured the advent of optical metamaterials, where the role of known, ordinary constituents of matter (atoms, ions, or molecules) is bestowed upon artificial "meta-atoms"—nanosized objects purposely designed to have the desired optical properties [1]. If the meta-atoms are much smaller than the wavelength of light interacting with them, then the meta-atom assembly, or an artificial composite metamaterial, would exhibit the desired properties macroscopically. The elegance of the metamaterials concept lies in the nearly limitless variety of meta-atom shapes and compositions, surpassing the variety of naturally occurring atoms, molecules and crystals (and, in turn, of natural materials).

The hallmark success of optical metamaterials is the design of artificial materials with optical properties that do not exist in naturally occurring media, such as negative refractive index [2]. Such negative-index media came out as seminal to the metamaterials field because of the vision of the "perfect lens" [3], where a slab of an artificial material with $n = -1$ (a "superlens") would focus light tighter than diffraction would allow in a conventional optical system. Even though this "perfect lens" dream, which hinges on the existence of lossless and isotropic negative-index metamaterials, may never come true, it did give birth to the entire field of study with several convincing experimental demonstrations of subwavelength imaging [4–7]. It was understood that the operating principle of the superlens is its ability to transmit, rather than to lose, the near-field information about a subwavelength object [8], as seen in Figs. 1(a)–1(c).

Later studies have shown that so-called *hyperbolic metamaterials* (HMMs) [9], which are extremely anisotropic media that are metal-like along some coordinate axes and dielectric-like along others, make it possible to do more—to convert the near field of an object into a set of propagating waves to be later imaged by conventional means. This concept of the hyperlens [10] [see Fig. 1(d)], followed by experimental demonstrations [11–13], showed that subwavelength imaging could be far closer to reality than one would assume after the initial disappointment in the negative-index superlens. This experimental success has sparked growing interest in the studies of hyperlenses and other metamaterials-based imaging devices (see the recent review [14] and references therein). In particular, studies have shown that a broad variety of structures, including metal-dielectric multilayers [15], possess the necessary requirements to function as a hyperlens. Such multilayers are of much simpler geometry than metamaterials commonly required to achieve the negative refractive index.

The existing designs of the hyperlens recover information both from propagating (referred to as low-k) waves with $k < n_a k_0$ and from evanescent (high-k) waves with $k > n_a k_0$ (where n_a is the ambient refractive index and $k_0 = \omega/c$). Such an approach is undoubtedly the best way of maximizing the output from the object to create the brightest possible subwavelength image. However, this approach has a serious downside: any propagating waves that exist in the object area but do not originate form the object (such as incident or stray light) would be transmitted, creating strong background in the image area. It is for this reason that existing demonstrations of the hyperlens focus on examples where background radiation can be eliminated. This is done either by imaging a subwavelength pattern in a metal screen [11,13,16,17] that covers the entire lens and blocks all incident light, or else by using self-illuminating objects such as fluorescent centers [18, 19]. In a scenario when objects to be imaged are weakly scattering and have to be illuminated by external light, as is very relevant in label-free biological imaging, a conventional hyperlens would be nearly useless because the resulting image would have extremely low contrast.

In this paper, we propose an alternative hyperlensing concept which is free from this downside and can provide high-contrast subwavelength images of weakly scattering objects. The proposed device only transmits high-k waves while blocking all propagating radiation from the object area [Fig. 1(d)], be it from the object itself or from elsewhere. The resulting image there-

#244021 Received 16 Jul 2015; revised 30 Aug 2015; accepted 7 Sep 2015; published 18 Sep 2015

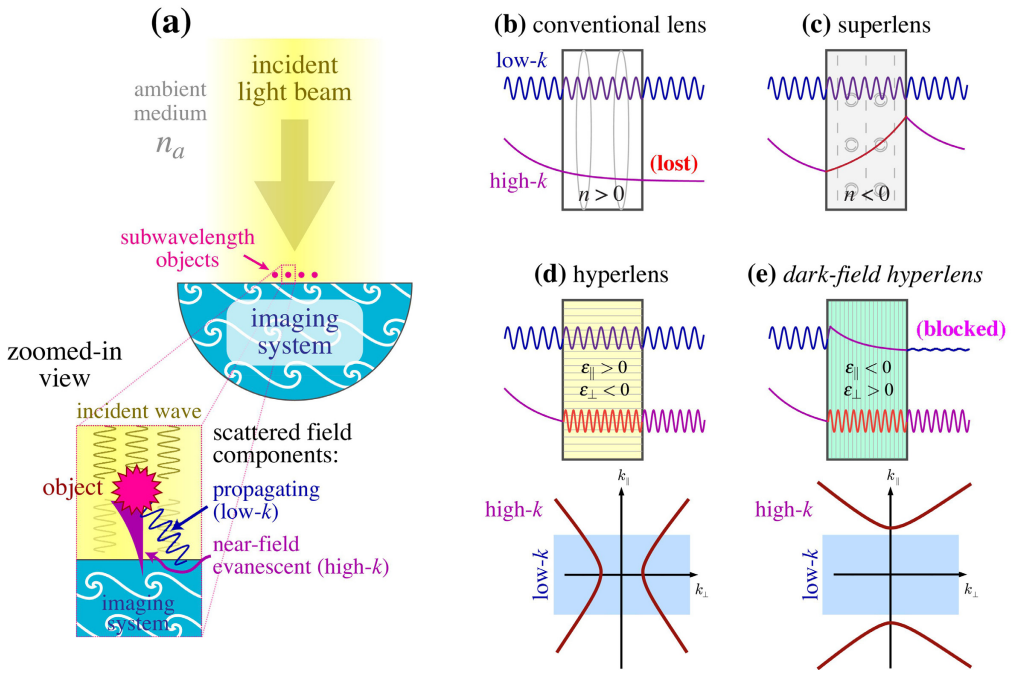

Fig. 1. (a) Overview of an optical imaging system with subwavelength resolution, schematically showing propagating low-k ($k < n_a\omega/c$) and evanescent high-k ($k > n_a\omega/c$) components of radiation scattered off subwavelength objects. (b–e) Schematics of how information contained in these components passes through different types of imaging systems. (b) *Conventional optical lens*: only the propagating low-k components are transmitted while the high-k evanescent waves carrying near-field information are lost, resulting in a blurred, diffraction-limited image. (c) *Superlens* [3]: high-k evanescent waves are amplified and the near-field information is recovered, enabling a subwavelength image, which nevertheless remains only in the near-field and cannot be reproduced by conventional optics. (d) *Hyperlens* [10]: high-k evanescent waves are converted to propagating waves using an HMM [9]; the resulting subwavelength image can therefore be seen in the far field, however its contrast against the background illumination will be poor if the object is weakly scattering. (e) *Proposed dark-field hyperlens*: using a modified kind of HMM [15] similarly couples the high-k evanescent waves to the far field but blocks the low-k propagating waves, filtering out the background illumination and allowing the subwavelength image contrast to be drastically enhanced. For the two kinds of hyperlenses, example dispersion relations are shown as insets in (d) and (e).

fore only contains information coming from subwavelength features of the sample, providing a much greater contrast than the conventional hyperlens. The proposed device relates to the conventional hyperlens in the same way as dark-field microscopy relates to conventional optical microscopy. Therefore we have termed the proposed device the *dark-field hyperlens* (DFHL), and the proposed concept, *dark-field superresolving optical microscopy*. Here, *superresolution* is understood as the ability to resolve images of subwavelength objects placed closer together than one half the wavelength of illuminating light, i.e., closer than the Abbe diffraction limit.

Our concept is distinct from the recently proposed scheme by H. Hu et al [20], where a plasmonic structure was used to increase the numerical aperture of the condenser lens of a conventional dark-field microscope. Another earlier work by H. Benisty et al proposed an alternative

#244021 Received 16 Jul 2015; revised 30 Aug 2015; accepted 7 Sep 2015; published 18 Sep 2015

design of plasmonic subwavelength imaging and coined the term dark-field hyperlens for the first time [21]. However, that design relies on application of two hyperlenses. One hyperlens is used for imaging the other is used to excite the sample in the confocal geometry. In contrast, in our approach the filtering of the background radiation is done by the imaging hyperlens itself. As a result, the device we propose is geometrically much simpler and within easier reach of modern fabrication facilities.

It should be stressed that beating the diffraction limit in the optical microscopy would constitute a major breakthrough in biological imaging because it neither requires special sample fixation and preparation techniques (such as electron-microscopy and scanning-microscopy methods) nor relies on special labeling (such as STED-like approaches [22]). As a result, the proposed dark-field superresolving optical microscopy can be used to obtain dynamic real-time images of weak-contrast subwavelength objects. Being able to see and investigate dynamic processes involving very small biological agents and macromolecules would be truly enabling to modern life sciences, as confirmed by the ongoing scientific efforts in search for such a technique [23–25]. Hence, the impact of such high-resolution, high-contrast, fast, and non-destructive subwavelength optical microscopy or nanoscopy—such as the DFHL is able to provide—can potentially be on par with the impact of the original invention of an optical microscope on biology several centuries ago. The accompanying possibility to reverse the operation of a hyperlens in order to selectively excite an object on a subwavelength scale may bring about an even greater advance in experimental biology, making it possible not only to observe the functioning of nanoscale biological agents, but also to actively interfere with them.

2. Results

2.1. Operating principle of the dark-field hyperlens

The primary physical concept behind subwavelength imaging in plasmonic metamaterials—the operating principle of the hyperlens—is the idea that a medium with extreme anisotropy, such that the components of the permittivity tensor have different signs, supports propagating waves with very large wave vectors. Indeed, we recall the dispersion relation for the extraordinary (TM-polarized) wave in a uniaxial birefringent medium

$$k_0^2 = \frac{\omega^2}{c^2} = \frac{k_\parallel^2}{\varepsilon_\perp} + \frac{k_\perp^2}{\varepsilon_\parallel}, \tag{1}$$

where $\varepsilon_\perp$ and $\varepsilon_\parallel$ are components of the dielectric permittivity tensor $\hat{\varepsilon} = \mathrm{diag}(\varepsilon_\parallel, \varepsilon_\parallel, \varepsilon_\perp)$; $k_\perp$ and $k_\parallel$ are respective components of the wave vector. We see that for weakly birefringent media the solutions of Eq. (1) in the k-space represent bounded shapes (ellipsoids), providing the upper limit on the possible values of k for propagating waves. In contrast, if the optical anisotropy is so strong that $\varepsilon_\perp$ and $\varepsilon_\parallel$ are of different signs, then the solutions of Eq. (1) change topology from bounded ellipsoids to unbounded hyperboloids, thus supporting propagating solutions with theoretically infinite wave vectors [26].

This fact had remained largely a theoretical curiosity until such hyperbolic dispersion could actually be realized for optical waves in HMMs—subwavelength metal-dielectric structures with rather simple geometries such as nanorod arrays and multilayers [9, 15]. It was shown that even though "infinitely large wave vectors" proved to be an idealization [27], HMMs can indeed support propagating plasmonic waves with very large k-vectors [28].

As a result, an HMM can transform high-k waves with $k_\parallel > n_a k_0$, which are evanescent in the ambient medium with refractive index n_a, into waves that can propagate through the metamaterial. To see how this gives rise to subwavelength imaging properties, we recall that any object's scattered field can be decomposed into a series of plane waves spanning the entire

#244021 Received 16 Jul 2015; revised 30 Aug 2015; accepted 7 Sep 2015; published 18 Sep 2015

range of k. The relation between the spatial representation of the object $f(x,y)$ and its image $g(x,y)$ in the Fourier optics approach is

$$g(x,y) = \frac{1}{(2\pi)^2}\iint_{-\infty}^{\infty} dk_x dk_y H(k_x,k_y) e^{-i(k_x x + k_y y)} \times \iint_{-\infty}^{\infty} dx' dy' f(x,y) e^{i(k_x x' + k_y y')}. \tag{2}$$

Here $H(k_x,k_y)$ is the transfer function of the imaging system, and it can be seen from the properties of Fourier transformation that $g(x,y) = f(x,y)$ (the image is perfect) if $H(k_x,k_y) = 1$. In conventional optics, propagation of light over some distance d in the ambient medium introduces a low-pass filter in the k-space, resulting in the transfer function $H_0(k_x,k_y) \propto \exp(-idk_\perp) = \exp\left(-id\sqrt{n_a^2 k_0^2 - k_\parallel^2}\right)$ with $k_\parallel^2 = k_x^2 + k_y^2$. Therefore, if the object's Fourier image is significantly extended into the area with $k_\parallel > n_a k_0$, or in other words, if the size of the object is smaller than the wavelength of light $\lambda = 2\pi/n_a k_0$, then all the components with $k_\parallel > n_a k_0$ (the near-field information) are lost [see Fig. 1(b)], and the image becomes blurred.

This low-pass filtering is overcome in HMMs, where Eq. (1) results in the expression

$$k_\perp = \sqrt{\varepsilon_\parallel k_0^2 - (\varepsilon_\parallel/\varepsilon_\perp) k_\parallel^2}, \tag{3}$$

which can remain real for very large $k_\parallel$ because $\varepsilon_\parallel/\varepsilon_\perp < 0$. This makes the transfer function such that the loss of near-field information is prevented [see Fig. 1(d)]. Thus, placing an HMM close to the object facilitates superresolution imaging.

This idea, combined with the use of curvilinear geometry so that high-k waves inside the metamaterial can be further coupled to outside propagating waves and imaged by a conventional lens, was put to use in the practical realization of the hyperlens [11]. Later studies followed with experimental demonstration of a spherical hyperlens at visible frequencies [16] and the design of an all-dielectric hyperlens [29], as well as with applications of the hyperlens design to other platforms such as terahertz [19] and acoustic [18] waves.

Depending on the signs of the eigenvalues in the dielectric permittivity tensor, hyperbolic media can be classified as either type I ($\varepsilon_\perp < 0 < \varepsilon_\parallel$) or type II ($\varepsilon_\parallel < 0 < \varepsilon_\perp$) [30]. In the periodic metal-dielectric multilayer geometry, the effective permittivity components can be obtained from the Maxwell-Garnett homogenization approach with [27]

$$\varepsilon_\parallel = \rho\varepsilon_m + (1-\rho)\varepsilon_d, \quad \varepsilon_\perp = \left[\rho\varepsilon_m^{-1} + (1-\rho)\varepsilon_d^{-1}\right]^{-1}, \tag{4}$$

where $\rho = d_m/(d_m + d_d)$ is the filling fraction of the metal. Therefore, by choosing the thicknesses of metal and dielectric layers in the stack (d_m and d_d), as well as the permittivities of metal and dielectric (ε_m and ε_d), one can eventually design a structure that is effectively either type-I or type-II HMM.

The key difference between the two types of HMMs can be seen from Eq. (1): the dispersion contour in the wave vector space has a different topology, forming either one connected or two unconnected hyperboloidal surfaces (see Fig. 2 for example structures). As a result [see Eq. (3)], type-I HMMs support bulk propagating waves with *any* value of the tangential wave vector $k_\parallel$, and act like dielectrics for TE-polarized (ordinary) waves. In contrast, type-II HMMs only support TM-polarized bulk propagating waves for $k_\parallel > k_{\text{cutoff}} = \sqrt{\varepsilon_\perp} k_0$, exhibiting effective metallic properties for lower $k_\parallel$ as well as for the TE-polarized waves.

It is worth noting that the hyperboloid-shaped dispersion contours lead to the preferential direction of propagation for high-k waves, given by the preferential orientation of the group velocity vector pointing normal to the dispersion curves (see insets in Fig. 2). This typically

#244021 Received 16 Jul 2015; revised 30 Aug 2015; accepted 7 Sep 2015; published 18 Sep 2015

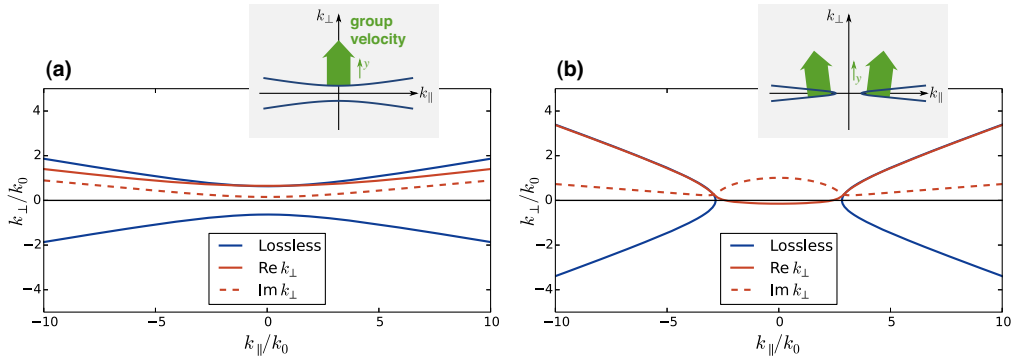

Fig. 2. Two-dimensional dispersion relation for (a) type I hyperbolic metamaterial (dielectric permittivity tensor components being $\varepsilon_\parallel = 0.36$, $\varepsilon_\perp = -13.31$) and (b) type II hyperbolic metamaterial ($\varepsilon_\parallel = -1.06$, $\varepsilon_\perp = 8.09$) The insets schematically show the direction of the group velocity for waves in certain parts of the k-space; for the type I hyperbolic metamaterial, it is possible that the majority of lower-k waves propagate in the y-direction (the canalization regime). Only one branch for $k_\perp$ is shown in the lossy case to aid the visual comparison with the lossless case.

causes waves from a point-like source or scatterer to propagate in a characteristic cone-like pattern [31, 32]. It is very often beneficial to tune the dispersion relations in such a way that this cone-like pattern becomes very narrow (almost line-like), which is called the canalization regime [32–37]. This regime ensures that high-k wave packets from different parts of the object remain spatially separated throughout their propagation in the hyperlens, making the subwavelength image formation more straightforward [34].

Consider now a scenario where there is a subwavelength object placed in front of an HMM-based hyperlens and illuminated by external light. At first sight, a type-I HMM is much better suited for the design of the hyperlens because it transmits both propagating components of the scattered radiation (with $k_\parallel < n_a k_0$) and all the evanescent components (with $k_\parallel > n_a k_0$, where n_a is the refractive index of the ambient medium). As a result, the subwavelength image with maximum resolution can be formed. However, a type-I HMM transmits the propagating low-k components originating not only from the object, but also from other sources, such as incident or stray light. Therefore, if the object to be imaged is weakly scattering (as is the case with most subwavelength objects made of dielectrics, such as all biological objects), the resulting image would have very low contrast, rendering such a hyperlens extremely difficult in use.

What we propose as the main idea of this paper is to modify the hyperlens in such a way that a type-I HMM is replaced with a type-II one designed so that k_{cutoff} exceeds $n_a k_0$. This filters all low-k propagating components, so that only the high-k waves stemming from the objects to be imaged can make it to the image area. Such a device in some sense represents the "inverse" of the conventional optics [compare Figs. 1(b) and 1(e)], introducing high-pass rather than low-pass filtering in the transfer function of the hyperlens.

To see that such high-pass filtering still allows a subwavelength image to be formed, we rewrite Eq. (2), reducing it to one dimension (assuming $k_\parallel = k_x$) for simplicity:

$$g(x) = \frac{1}{2\pi}\int_{-\infty}^{\infty} dk_x H(k_x) e^{-ik_x x} \int_{-\infty}^{\infty} dx' \Pi(x/D) e^{ik_x x'}, \tag{5}$$

where the object of size D is represented by the rectangular (unit box) function $\Pi(x)$ that assumes the unity value for $-1/2 < x < 1/2$ and zero value elsewhere. In this formalism, the high-pass filtering action of the type-II HMM blocking all the waves below k_{cutoff} can be mod-

#244021 Received 16 Jul 2015; revised 30 Aug 2015; accepted 7 Sep 2015; published 18 Sep 2015

elled by assuming the transfer function $H(k_\parallel) = 1 - \Pi(k_\parallel/k_{\text{cutoff}})$ [see Fig. 3(a)], which results in the image of the form

$$g(x) = \Pi\left(\frac{x}{D}\right) - \frac{1}{\pi}\left[\text{Si}\left(\frac{D-2x}{4}k_{\text{cutoff}}\right) + \text{Si}\left(\frac{D+2x}{4}k_{\text{cutoff}}\right)\right], \tag{6}$$

where $\text{Si}(x) = \int_0^x \text{sinc}(t)dt$ is the sine integral function. We see that the high-pass filtering retains the presence of the image in the form of the first term in Eq. (6), the second term adding some background to the image as seen in Fig. 3(b). This is unlike the action of the low-pass filtering induced by propagation in some isotropic ambient medium, which can be modelled by similarly assuming the box-type transfer function $H_a(k_\parallel) = \Pi(k_\parallel/n_a k_0)$ and results in

$$g_a(x) = -\frac{1}{\pi}\left[\text{Si}\left(\frac{D-2x}{4}n_a k_0\right) + \text{Si}\left(\frac{D+2x}{4}n_a k_0\right)\right], \tag{7}$$

which becomes increasingly blurred as $n_a k_0 D$ decreases to values significantly below unity.

Therefore, we conclude that the image formed by a hyperlens based on the type-II rather than type-I HMM would still be subwavelength as per Eq. (6), but would have a greatly enhanced contrast compared to the conventional hyperlens because the object-unrelated background, such as signal stemming from the incident light, is blocked. Specifically, the subwavelength image contrast, which can be defined as the visibility

$$\begin{aligned} V_{\text{sub}} &= \lim_{\delta\to 0}\frac{|g(D/2-\delta)| - |g(D/2+\delta)|}{|g(D/2-\delta)| + |g(D/2+\delta)|} \\ &= 1 - 2\left[1 + \left|\frac{\pi}{\text{Si}(k_{\text{cutoff}}D/2)} - 1\right|\right]^{-1}, \end{aligned} \tag{8}$$

can be seen to approach unity as the object size (or more precisely, $k_{\text{cutoff}}D$) decreases.

We can see that the proposed hyperlens modification is similar in spirit to dark-field microscopy, where background illumination is blocked and only the information coming from the specimen is isolated. Therefore, we call the proposed hyperlens based on the type-II HMM the *dark-field hyperlens* (DFHL), and will by contrast refer to the conventional hyperlens with type-I HMM as the bright-field hyperlens (BFHL).

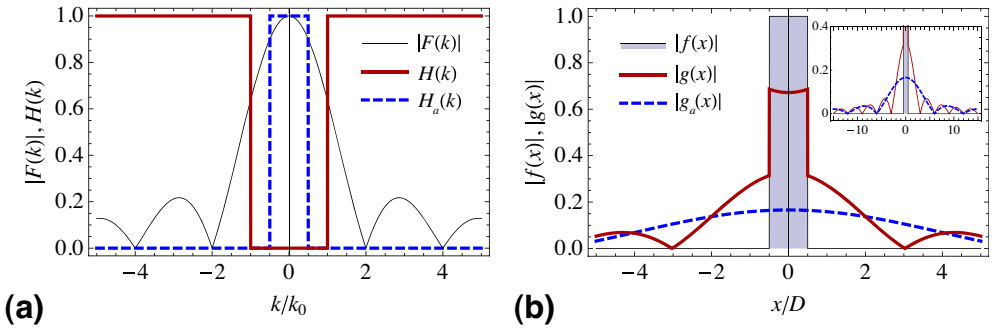

Fig. 3. Subwavelength imaging properties of the DFHL: (a) The Fourier transform $F(k)$ of a subwavelength object given by $f(x) = \Pi(x/D)$ with $D = \lambda/2$, overlaid with example transfer functions of the ambient medium $H_a(k)$ (low-pass filtering) and of the DFHL $H(k)$ (high-pass filtering). (b) Comparison between the images of an object with the size $D = \lambda/6$ obtained by Eq. (6) (solid line) and Eq. (7) (dashed line) with $n_a = 1$ and $k_{\text{cutoff}} = 2k_0$, respectively. The shaded area shows the object $f(x)$ itself. The inset shows the same plot zoomed out in the x axis to show the sinc dependence in $g_a(x)$.

#244021 Received 16 Jul 2015; revised 30 Aug 2015; accepted 7 Sep 2015; published 18 Sep 2015

2.2. Planar structure with hyperbolic dispersion (the "poor man's" dark-field hyperlens)

To demonstrate the proposed concept and to compare the functionality of DFHL and BFHL, we simulated light propagation in a scenario where two subwavelength metallic scatterers are placed in front of planar structures with hyperbolic dispersion (PSHD). The scatterers are separated by a distance shorter than half the wavelength of the plane wave incident on them; the existence of two resolvable images under these conditions would signify the presence of superresolution. The planar geometry is chosen for simplicity, and we can call such a structure the "poor man's DFHL" because such a design is only able to transmit a subwavelength image of an object some distance without true magnification, by the same token as a slab of metal is dubbed "the poor man's superlens" [38]. However, despite the obvious drawbacks of this "toy model", it is useful as a proof-of-principle that can demonstrate the operating principle of the proposed DFHL without having to regard features brought about by more complicated designs.

The structures are multilayers made of alternating metal and dielectric layers, with 2×50 layers in total. All layers have 10 nm thickness, and the BFHL and DFHL structures differ by the material parameters of the metal and dielectric used. Figure 2 shows the corresponding dispersion properties in the effective medium limit with and without losses. The exact dispersion relation given by Bloch's theorem is very close to their effective medium counterparts due to the large size ($k/k_0 = 35.75$) of the Brillouin zone imposed by the finite layer thickness [27,28]. COMSOL finite element software was used in the numerical simulations. We adopted the supercell approach, when the simulation domain was made periodic in the x direction (tangential to the layers, see Fig. 4), in order to avoid numerical errors arising from metal layers terminating inside perfectly-matched layers (PML) region. To prevent artifacts arising from interaction between the scatterers from different supercells, we made the width of the simulation domain 5 μm, so any periodicity effects were expected to be negligible. In the y direction (normal to the layers), absorbing boundary conditions were used, with 200 nm thick PMLs placed 1 μm away from the multilayer. A normally incident plane wave with wavelength 715 nm was impinging on the hyperlens from the ambient medium with refractive index $n_a = 1$, excited in the simulation by surface current boundary condition. On the other side of the multilayer, a substrate with artificially high refractive index ($n_s = 10$) was placed so that high-k waves remain propagating, and the subwavelength image pattern could be visualized.

The results of the simulations are shown in Fig. 4. As expected, Fig. 4(a) shows that the BFHL transmits a significant portion of the incident plane wave with $k_{\|} = 0$, which creates a strong background in the image area. The images of the objects are manifested as faint "shadows" where the intensity of the background is reduced due to scattering by the objects. We see that even though the two subwavelength images are well-resolved (in agreement with the operating principle of the hyperlens), the image contrast is sufficiently low even for relatively strongly scattering objects such as metallic spheres. To quantify the contrast, we define the bright-field image visibility in the same spirit as in Eq. (8) as the contrast between the on-image and between-images field intensities: $V_{\mathrm{BF}} = |I_{\min} - I_0|/(I_{\min} + I_0)$, where $I_{\min}$ is the field intensity at the dip corresponding to each image, and I_0 is the intensity at the peak between the dips (at $x = 0$), which is almost equal to the background intensity. From Fig. 4(a) it can be recovered that $V_{\mathrm{BF}} = 0.14$.

In contrast, Fig. 4(b) shows that the DFHL reflects the incoming plane wave almost completely, resulting in no background in the image area. Only the subwavelength high-k components of the scattered field are transmitted via coupling to bulk plasmonic waves inside the HMM, predominantly in the form of characteristic cone-like patterns [31] arising because the normals to the isofrequency surface in the dispersion relation Eq. (1) have a preferred direction [see inset in Fig. 2(b)]. Each scatterer produces its own distinct cone pattern, which propagates independently in the hyperlens. As a result, a clearly visible and recognizable subwavelength

#244021 Received 16 Jul 2015; revised 30 Aug 2015; accepted 7 Sep 2015; published 18 Sep 2015

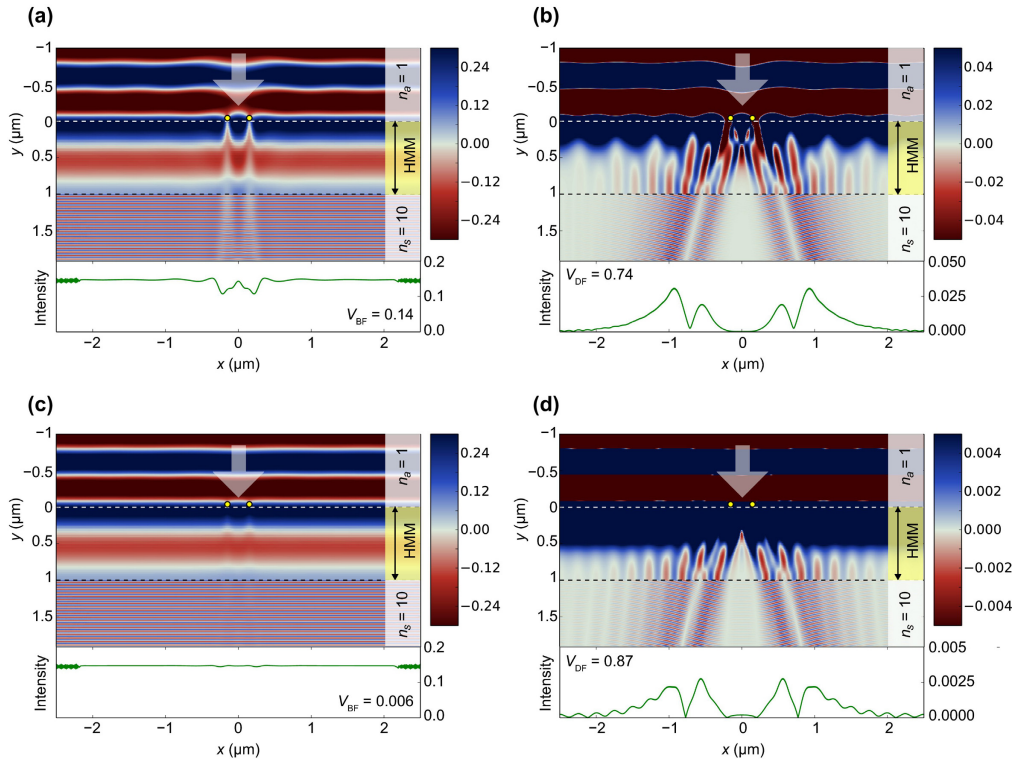

Fig. 4. (a–b) Full-wave frequency-domain simulation of a plane wave ($\lambda = 715$ nm) impinging on two metallic scatterers (diameter 70 nm, $n = 0.01 + 1.5i$), placed 300 nm apart, in front of planar structures with hyperbolic dispersion (a) conventional bright-field and (b) proposed dark-field structures. Both structures are alternating metal-dielectric multilayers containing a total of 100 layers with 10 nm thickness and material parameters $n_m = 0.154 + 1.589i$, $n_d = 1.794$ (type-I HMM) and $n_m = 0.14 + 2.06i$, $n_d = 1.45$ (type-II HMM) for the BFHL and DFHL, respectively. The area behind the structures contains a high-index medium ($n_s = 10$). (c–d) Same as (a–b) but for dielectric scatterers ($n = 1.5$). The lower plots (green lines) show the x-dependence of the field intensity 700 nm behind the planar structure ($y = 1700$ nm).

image pattern is formed at the far end of the planar structure. In contrast to the bright-field structure operated in the canalization regime, the image is no longer placed directly in front of the objects but is laterally shifted, forming two pairs of image points where each of the pairs can be regarded as a stand-alone subwavelength image. Comparing the plots of light intensity in the image area ($y = 1700$ nm), we can see that the DFHL produces an image with much lower brightness but with much higher contrast than the BFHL. Similarly introducing the visibility as the contrast between the on-image and between-images field intensities, we define $V_{\mathrm{DF}} = (I_{\mathrm{peak}} - I_{\mathrm{dip}})/(I_{\mathrm{peak}} + I_{\mathrm{dip}})$ where I_{peak} is the field intensity at the weaker of the two image peaks and I_{dip} is the intensity at the dip between the peaks. From Fig. 4(b) we can see that $V_{\mathrm{DF}} = 0.74$, much higher than the corresponding V_{BF} obtained with a BFHL.

Thus the main advantage of the DFHL, namely its suitability for subwavelength imaging of weak scatterers, is clearly demonstrated in Fig. 4. Moreover, we note that the metallic particles used in the presented example form rather strong scatterers. Using dielectric particles as objects, as is relevant in label-free biological imaging, would further bring out the advantage

#244021 Received 16 Jul 2015; revised 30 Aug 2015; accepted 7 Sep 2015; published 18 Sep 2015

of high-contrast imaging facilitated by the DFHL. Indeed, Figs. 4(c) and 4(d) shows that the image in the BFHL almost vanishes, becoming indistinguishable against the background of the incident wave, while the DFHL retains the imaging capability. The corresponding visibilities are $V_{\mathrm{BF}} = 0.006$ and $V_{\mathrm{DF}} = 0.87$, i.e., a DFHL produces an image with more than 140 times better contrast that a BFHL. On the other hand, this contrast enhancement comes at the cost of further decreasing the image brightness [compare the scales in Figs. 4(d) and 4(b)], which has a downside of making noise and other artifact features more visible. One of such features is a visible oscillation pattern in the DFHL case. This pattern originates from the wave fronts having near-parallel orientation with respect to their propagation direction inside the dark-field PSHD, which in turn results from the hyperbolic dispersion (see insets in Fig. 2).

2.3. Cylindrical-geometry dark-field hyperlens

As discussed in the previous section, the planar-geometry structure is only capable of transmitting the information encoded in the high-k components of radiation scattered off a subwavelength object through the multilayer thickness, but it is not able to perform any actual magnification. The reason is twofold. First, as seen in Fig. 4(b), the image points end up being the same distance apart as the original objects, so such a subwavelength image cannot be further processes by conventional optics. Second, the high-k components propagating in the HMM would still be highly evanescent in any naturally occurring media, which made it necessary to use a fictitious medium with unrealistically high refractive index ($n_s = 10$) in order to outcouple these components out of the lens in Fig. 4; repeating the calculations for $n_s = 1$ actually showed that there is no far-field subwavelength image. (We note that the outcoupling issue is a special challenge for a DFHL because, unlike the BFHL case, all the waves pertaining to the image formation by the DFHL are high-k waves.)

Both these problems are conventionally solved by employing a cylindrical [10] or spherical [16] geometry. The objects to be imaged are placed at the inner surface of the circular DFHL, and the high-k waves travel outward towards the outer surface. This gradual geometric transformation, sometimes combined with a gradient imposed on the layers thickness as one moves outward, serves to increase the distance between the image points compared to the distance between the objects, and at the same time, impose transformation on waves existing inside the hyperlens in such a way that $k_{\|}$ becomes smaller as one moves away from the center of the cylinder, which is a feature of the cylindrical anisotropy [10]. Therefore the image-forming waves can be coupled out of the hyperlens and subsequently captured by conventional optics.

We have adapted the design principles elaborated in the previous section to the curvilinear geometry, starting with a multilayer structure similar to one used in Fig. 4(b) (2×50 layers in total) and making the individual layer thickness 15 nm. The larger layer thicknesses were chosen in order to increase the total thickness of the lens, thereby increasing the magnification factor of the structure. Material parameters were also slightly modified ($n_m = 0.14 + 2.26i$, $n_d = 1.45$) in order to adjust the cone angle of the propagating waves inside the DFHL in such a way as to illustrate the field distribution patterns more clearly. The layers form concentric cylindrical shells with inner radius 1000 nm and outer radius 2500 nm. The simulation set-up is similar to the demonstration of the planar structure except that the ambient medium around the lens is now realistic with $n_s = 3$. Since the cylindrical structure is spatially finite (as opposed to the infinite plane multilayer), the supercell approach was no longer needed, and hence absorbing boundary conditions were used on all sides. In order to avoid numerical artifacts arising from the interaction of high-k waves with PMLs, complete circular structure was enclosed in the simulation domain while only the upper half-cylinder was considered as the useful structure; the presence of losses in the HMM structure was expected to prevent the effects of round-trip wave propagation in the structure. As before, the objects to be imaged were subwavelength-

#244021 Received 16 Jul 2015; revised 30 Aug 2015; accepted 7 Sep 2015; published 18 Sep 2015

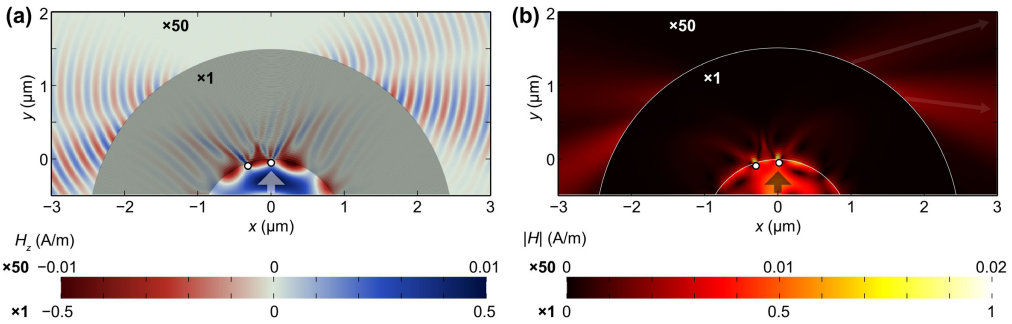

Fig. 5. Cylindrical-geometry DFHL: numerical results showing (a) field map and (b) field intensity map for a beam incident on two subwavelength scatterers, 70 nm in diameter and 290 nm apart, in front of a DFHL with cylindrical geometry. The structure consists of 2×50 layers with thickness 15 nm and $n_m = 0.14 + 2.26i$, $n_d = 1.45$; the inner and outer radius of the structure is 1000 and 2500 nm, respectively. To simultaneously show the field before, inside, and after the hyperlens, the color scale of the fields after the hyperlens is magnified by 50.

sized cylinders placed close to the inner surface of the hyperlens. They were illuminated by a beam with wavelength 715 nm and spatial FWHM 0.67 μm in the $+y$ direction (see Fig. 5); in the simulation set-up used, such excitation was created by placing a surface current source in the middle of the hyperlens.

The results are shown in Fig. 5. The field distribution map [Fig. 5(a)] shows that the operation is quite similar to the PSHD considered above, with each object giving rise to a cone-like pattern in the hyperlens. However, the high-k waves in these patterns are now transformed as they propagate outward, and can therefore be coupled out of the lens if the output medium has a realistic refractive index. This can be confirmed by the intensity map [Fig. 5(b)], where each object is seen to produce a pair of beams in the output medium; one notices that the right-hand side beams have slightly better visibility due to the asymmetric placement of scatterers with respect to the direction of the incident wave. It can also be seen that the geometric transformation makes the distance between the image beams greater than between objects (e.g. about 800 nm for 290 nm separation between objects), making the resulting subwavelength image suitable for further processing by conventional optics. We stress that two well-resolved image peaks have been numerically observed for the distance between the objects smaller than $\lambda/2 = 357.5$ nm, which means that our demonstration satisfies the criterion for super-resolution imaging.

To further characterize the hyperlensing functionality of the proposed structure, we vary the distance between scatterers and analyze how this variation affects the fields in the image area. The results are presented in Fig. 6. Bringing the scatterers closer together causes a corresponding decrease in the distance between the points where the image beams emerge from the hyperlens [Fig. 6(a)]. Decreasing the distance further makes the image beams indistinguishable, signifying that the resolution limit is reached, although Fig. 6(a) shows that the two radiation cones are still distinct inside the hyperlens. The distance between the centroids of image beams nearly proportional to the distance between objects [Fig. 6(b)], and it can be seen that well-resolved images can be formed for objects placed 175 nm apart from each other. However, the quality of the image is seen to deteriorate for distances lower than 300 nm, with the fluctuating visibility of the image that prevents the two image points from being resolved at some values of the inter-object separation. These fluctuations result from the interference of high-k patterns inside the hyperlens. Above 300 nm separation, the subwavelength imaging functionality of the proposed hyperlens is fairly reliable. Overall, the magnification factor was found to be around

#244021 Received 16 Jul 2015; revised 30 Aug 2015; accepted 7 Sep 2015; published 18 Sep 2015

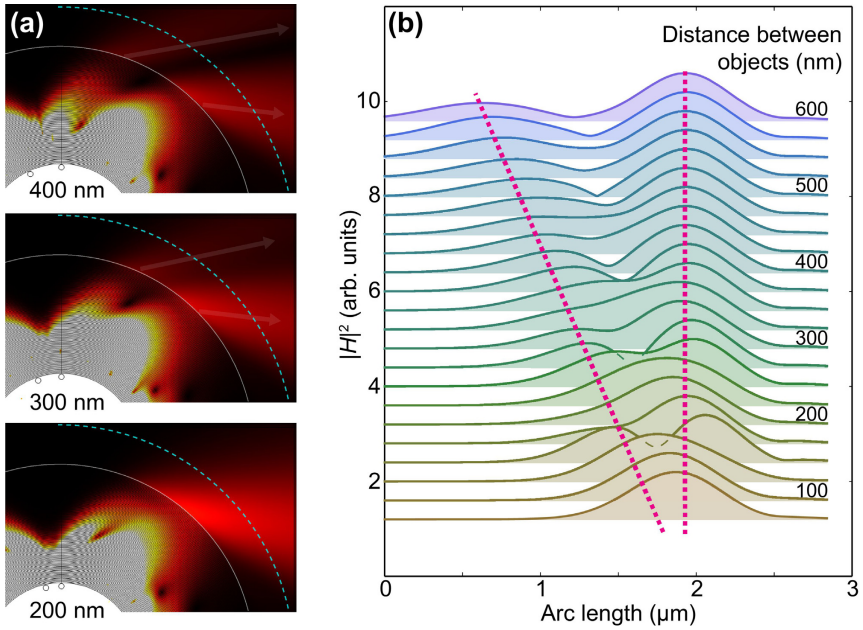

Fig. 6. Operation of the DFHL under different object separation. (a) Intensity maps similar to Fig. 5(b), cropped to show the right-hand side image, for three different values (400, 300 and 200 nm) of the distance between the subwavelength scatterers. (b) Dependence of the field intensity behind the the hyperlens (500 nm behind its outer surface, shown by the dashed line in the intensity plots) for the distance between objects varying between 75 and 600 nm in 25-nm steps; dotted lines are a guide to the eye showing the theoretical location of the image points in the absence of interference effects between high-k cones.

2.5, which is near the limit for a DFHL made of layers with a constant thickness. Variable thickness structures, where the gradient imposed on the layer thickness provides additional k-vector transformation, may achieve higher magnification.

3. Discussion

On the way from the presented numerical demonstration of the DFHL functionality to the experimental realization, it is worth pointing out a few tradeoffs and limitations involved in the proposed DFHL design. The key tradeoff is the operating width of the area in the k-space that contributes to the image formation. On the one hand, the DFHL should allow propagation of a broad range of high-k waves near its inner surface while having strong attenuation for low-k waves, so that the subwavelength image is extracted and separated from background radiation. On the other hand, the waves at the outer surface should have sufficiently low k-vectors in order to pass through to the surrounding medium. This tradeoff fundamentally narrows down the range of high-k waves taking part in the image formation, which in turn limits the imaging resolution according to Fig. 3(b), and gives rise to the requirement that n_s must be greater (in our examples, much greater) than n_a. Relaxing this requirement as much as possible may be achievable through further optimization of the hyperlens geometry, which is a subject of future investigations.

Similar considerations dictate that the hyperlens thickness needs to be chosen carefully, especially in presence of material losses. Choosing a thick multilayer would attenuate the useful signal, making the image too weak, whereas a very thin structure would frustrate the filtering

#244021 Received 16 Jul 2015; revised 30 Aug 2015; accepted 7 Sep 2015; published 18 Sep 2015

properties with respect to the low-k components, so part of the background radiation would still get through and reduce the imaging contrast. This tradeoff is worsened by the adverse effects of material losses, which are greater on the high-k waves than on the low-k waves [39]. Yet another related tradeoff is the choice of the value of k_{cutoff} in the design of the underlying multilayer. If it is too close to $n_a k_0$, the low-k components become less attenuated, while higher k_{cutoff} prevents part of the high-k information from forming an image and thus harms both contrast and resolution [see Eq. (8) and Fig. 3(b)]. So, it follows that lowering losses should be the priority optimization direction for the DFHL, and one may eventually resort to active loss compensation using gain media [40, 41]. Another promising strategy is to consider the DFHL operation in the mid-infrared range, where low-loss semiconductor materials are available [42, 43].

Taken together, the loss-related factors place a limit of $2.5\ldots3$ on the magnification factor of the cylindrical DFHL achievable by geometrical transformation alone. A different challenge is related to each scatterer producing a cone-shaped pattern within the hyperlens, which poses little difficulty in the considered 2D simulations but requires post-processing to reconstruct the image in the 3D case. It is for this reason that a hyperlens is usually made to operate in the canalization regime [34, 35]. The type-I HMM underlying the BFHL naturally tends to near-canalization regime [see Fig. 4(a)] for sufficiently flat dispersion relation because its topology enforces the group velocity of many lower-k components to point towards $k_\perp$. In contrast, the type-II HMM in the DFHL shows the opposite behavior [see the insets in Fig. 2]. Besides, flattening the dispersion relation (by scaling $\varepsilon_\parallel$) further reduces the attenuation of low-k waves, as can be seen by solving Eq. (1) for $k_\parallel = 0$ and yielding $\mathrm{Im}(k_\perp) \approx k_0\sqrt{-\mathrm{Re}\,\varepsilon_\parallel}$ in the limit of small material losses. So, designing the DFHL in the canalization regime remains a challenge, and the proposed examples are chosen to operate well outside this regime [see Figs. 4(b) and 4(d) and Fig. 5]. In the cylindrical geometry, it still remains an open question how to choose the aperture angle of the cone-like patterns to minimize the interference effects seen in Fig. 6 in order to optimize the imaging resolution.

Nevertheless, we stress that the presented simulation results only constitute the proof-of-principle for the proposed DFHL concept. It is therefore expected that further optimization can improve the DFHL imaging performance. For example, a higher magnification and better image quality may be possible with gradient structures where layer thicknesses vary across the thickness of the lens, although such a structure would be more difficult to manufacture. Another promising optimization direction is to combine two hyperlens structures (BFHL and DFHL) in one device, along the same lines as a combination of a superlens and a hyperlens suggested earlier [17]. In such a hybrid device, the DFHL would perform preliminary magnification along with background radiation filtering, after which the BFHL would carry out the main magnification in the canalization regime.

We also note that the we have deliberately chosen the structures with deeply subwavelength layers (10–15 nm for λ=715 nm) in order to ensure the relatively good applicability of the effective medium approximation throughout a significant range of high-k waves shown in Fig. 2. In structures with thicker layers, effects originating from the deviation of the exact Bloch-theorem dispersion from its effective medium counterpart are expected to be pronounced [27, 28]. The detailed analysis of the influence of these effects on the imaging properties of the DFHL should be a subject of future research. Finally, generalizing the DFHL operation to a finite frequency range rather than a single wavelength is a promising direction for further studies; the non-resonant character of hyperbolic metamaterials [13] suggests that such generalization should be possible.

#244021 Received 16 Jul 2015; revised 30 Aug 2015; accepted 7 Sep 2015; published 18 Sep 2015

4. Conclusions

In summary, we have proposed a concept for high-contrast subwavelength imaging (hyperlensing) of weakly scattering objects through the use of type-II rather than type-I HMM in the hyperlens, which blocks all propagating waves existing in the object area. The proposed *dark-field hyperlens*, so termed because its operating principle is similar to suppressing incident light in dark-field optical microscopy [21], only transmits high-k waves stemming from subwavelength features of the sample (see Fig. 1). The resulting subwavelength image therefore has a much greater contrast than the one produced by a conventional hyperlens; in the presented numerical example the contrast enhancement by more that two orders of magnitude was demonstrated for subwavelength dielectric scatterers (see Fig. 4). Simulations further confirm the feasibility of the DFHL operation. We presented the proof-of-principle DFHL design, demonstrating its subwavelength imaging capability with weakly scattering objects illuminated by external light (see Fig. 5). This is in contrast with previous studies on the hyperlens [11, 16, 17] where the choice of the sample was intentionally made in such a way as to exclude background radiation.

In the bigger picture, the proposed concept of the *dark-field superresolving optical microscopy* can find many applications in biological imaging because it can be performed without the use of fluorescent markers and/or special sample preparation techniques. As a result, the proposed method can be used to obtain dynamic real-time images of weak-contrast subwavelength objects. The eventual possibility to see and investigate dynamic processes involving subwavelength-sized biological agents and macromolecules (including *in vivo* studies) can be enabling to modern life sciences. Moreover, the possibility to reverse the operation of a hyperlens, which can be realized by virtue of the time-reversal symmetry of the Maxwell equations [14], can be used to focus light in a subwavelength scale and selectively excite a subwavelength object. This may bring about an even greater advance in experimental biology, making it possible to actively interfere with nanoscale biological agents while observing them.

Acknowledgments

This work has received financial support from the People Programme (Marie Curie Actions) of the European Union's 7th Framework (EU FP7) Programme FP7-PEOPLE-2011-IIF under REA grant agreement No. 302009 (Project HyPHONE). One of us (T.R.) thanks the Archimedes Foundation for financial support (Kristjan Jaak scholarship).

#244021 Received 16 Jul 2015; revised 30 Aug 2015; accepted 7 Sep 2015; published 18 Sep 2015